PHILOSOPHICAL TRANSACTIONS A

rsta.royalsocietypublishing.org

Research



Cite this article: Barber T, Griffith WA. 2017 Experimental constraints on dynamic fragmentation as a dissipative process during seismic slip. *Phil. Trans. R. Soc. A* **375**: 20160002. http://dx.doi.org/10.1098/rsta.2016.0002

Accepted: 16 June 2017

One contribution of 6 to a Theo Murphy meeting issue 'Faulting, friction and weakening: from slow to fast motion'.

Subject Areas:

geophysics, geology, plate tectonics

Keywords:

faulting, dynamic rupture, fragmentation, pulverized rocks, frictional weakening, fracture energy

Author for correspondence:

W. Ashley Griffith e-mail: griffith.233@osu.edu

[†]Present address: School of Earth Sciences, Ohio State University, Columbus, OH 43210, USA.

Electronic supplementary material is available online at https://dx.doi.org/10.6084/m9. figshare.c.3832558.

THE ROYAL SOCIETY

Experimental constraints on dynamic fragmentation as a dissipative process during seismic slip

Troy Barber and W. Ashley Griffith[†]

Department of Earth and Environmental Sciences, University of Texas at Arlington, Arlington, TX 76019, USA

TB, 0000-0001-7210-9038

Various fault damage fabrics, from gouge in the principal slip zone to fragmented and pulverized rocks in the fault damage zone, have been attributed to brittle deformation at high strain rates during earthquake rupture. Past experimental has shown that there exists a critical threshold in stress-strain rate space through which rock failure transitions from failure along a few discrete fracture planes to intense fragmentation. We present new experimental results on Arkansas Novaculite (AN) and Westerly Granite (WG) in which we quantify fracture surface area produced by dynamic fragmentation under uniaxial compressive loading and examine the controls of pre-existing mineral anisotropy on dissipative processes at the microscale. Tests on AN produced substantially greater new fracture surface area (approx. $6.0 \,\mathrm{m}^2\,\mathrm{g}^{-1}$) than those on WG $(0.07 \,\mathrm{m}^2 \,\mathrm{g}^{-1})$. Estimates of the portion of energy dissipated into brittle fracture were significant for WG (approx. 5%), but appeared substantial in AN (10% to as much as 40%). The results have important implications for the partitioning of dissipated energy under extreme loading conditions expected during earthquakes and the scaling of high-speed laboratory rock mechanics experiments to natural fault zones.

This article is part of the themed issue 'Faulting, friction and weakening: from slow to fast motion'.

1. Introduction and background

(a) Introduction

The brittle damage process in rocks exhibits a strain rate dependence, passing through a critical high strain rate transition [1,2]. At lower strain rates, macroscopic failure is achieved via localized, throughgoing fractures, whereas high strain rates lead to pervasive, intersecting fractures and, eventually, bulk failure through intense fragmentation [1–5]. In nature, this fragmentation transition is evidenced by intensely comminuted rocks that are associated with fast strain rate events like earthquake rupture, explosive volcanic eruption and bolide impact, as well as events related to mining, military and excavation activities such as rock burst and explosive blasting. Under such impulsive loading conditions, rocks spanning a wide range of composition and grain size are often reduced to submicrometre-sized fragments, even when subjected to small total strain [6–8]. This has led several workers to interpret intensely fragmented rocks in fault damage zones as products of dynamic rupture propagation approaching, or in some cases exceeding, the shear wave speed [1,2,9–11], and a significant potential sink for energy dissipated during earthquake rupture [12]. Testing this last assertion has been difficult based on field observations alone.

Whereas rock fragmentation can occur in a single impulsive event, fault damage zones are the manifestation of numerous processes acting on faults throughout the seismic cycle [13]. Damage may be largely the result of pre-existing anisotropy [14]; it may form in the process zone of propagating cracks and slip pulses [15–17], or at geometric barriers or step-overs along discontinuous faults [18,19], or it may result from dynamic, transient loading during fast earthquake rupture [12,20,21]. Intense grain size reduction via wear and fragmentation has been shown experimentally to correspond with rapid weakening during the initial stage of unstable frictional slip and probably contributes to fault instability [22,23]. Some have conjectured that the production of fine-grained gouge may also constitute a major energy sink within the principal slip zone (psz) during the rupture process [6,12,24], although this conclusion is debated [7]. The recent identification [1,9,25] of wide swaths (tens to hundreds of metres) of what have been coined pulverized rocks that appear to have been shattered *in situ* has introduced an additional source of complexity in the interpretation of fault damage zone structures.

(b) Pulverized rocks

In this paper, we follow previous authors and adopt the term 'pulverized' rocks to describe a final damage product and not a particular mechanical process (i.e. fragmentation); specifically, we employ it in reference to fault damage zone rocks exhibiting texture and damage distribution distinctly different from the breccias and cataclasites characteristic of most fault damage zones. Microstructurally, pulverized rocks contain profuse and dense networks of microcracks. Grain size is pervasively reduced, often to the nanometric scale. Pulverized fault rocks also exhibit little evidence of shear or rotation of fragments, meaning that original rock fabrics and microstructures are recognizably preserved [6,7,9,25,26]. At the fault scale, pulverized rocks appear to be limited to shallow crustal depths and often exhibit an asymmetric damage pattern about the fault plane, preferring formation in the *stiffer* fault blocks [7,9,25,27,28], an observation consistent with models of rupture along a bimaterial interface [29].

Several outstanding questions with regard to pulverized fault rocks include: (i) *How much energy is consumed in producing the extensive fracture surface area indicative of pulverized rocks, and how is that energy distributed over multiple seismic cycles?* The consensus on the portion of the dissipated energy during earthquakes consumed in creating fracture surfaces is approximately 1% [7,26,30], but some studies indicate that this work can be as great as 50% [6,12]. Recent work has attributed an apparent break in scaling between breakdown work in high-speed rock friction tests to fracture energy from seismological records of earthquakes. In particular, Nielsen *et al.* [31] showed that the fracture energy calculated as the work done during the frictional weakening process in rotary shear tests (G_f) closely corresponds to the seismologically determined fracture energy from natural earthquakes (G') for events with slip between 1 cm and 1 m (approx. $3 \le M_w \le 7$), but for larger events G_f underestimates G'. They ascribed this discrepancy to energy dissipation due to inelastic off-fault yielding, which is expected to increase with increasing rupture size [31,32]. Therefore, it is possible that intense grain size reduction via fragmentation, both within the psz and throughout the greater fault damage zone, may indeed constitute a significant

portion of the energy dissipated during large earthquakes. (ii) What micromechanical processes contribute to the intense comminution evident in pulverized rocks? Whereas past experimental work had delineated critical strain rate and stress thresholds for the transition to fragmentation, the physical mechanisms for pulverization of fault rocks, particularly as they affect earthquake propagation and frictional slip, are less well understood. Commercial crushing and grinding operations [33], as well as laboratory and field studies of rock deformation [8], indicate the existence of a mineral-specific, minimum possible grain size attainable via fracture under quasistatic compressive loading (i.e. a grind limit), a result supported by fragmentation models [34,35]. However, tensile loading or compressive loading at very high (approaching shock) strain rates may produce further comminution [35]. (iii) Beyond critical stress and strain rate thresholds, what aspects of loading history govern the transition to rock fragmentation, and what can these controls reveal about the rupture and slip processes on natural faults which contribute to their formation and, more importantly, to frictional weakening processes during earthquakes? In extending our understanding of fragmentation processes in rocks beyond simply recognizing the products of dynamic rupture in the rock record [36], and the feedbacks between fragmentation and earthquake rupture, it is necessary to develop a well-constrained model of fragmentation mechanics, including the relationship between load history (e.g. tension, compression, number of load cycles and loading pulse duration) and the degree of fragmentation, and the dissipated energy involved in this fragmentation.

Here, we take a step in this direction by studying the effect of mineralogy on the rate-dependent fragmentation transition under dynamic uniaxial compression, as well as the degree of comminution that occurs across this transition, with particular focus on the energy sink represented by this process. We also explore the role of fragmentation in frictional weakening, as well as the challenge of scaling these experimental results to natural fault rocks.

(c) Laboratory constraints on dynamic fragmentation

Experimental studies of dynamic rock fragmentation have been conducted primarily using the split Hopkinson pressure bar (SHPB), a device by which rock samples are loaded by a transient uniaxial compressive pulse under strain rates between 10^1 and 10^3 s⁻¹ [3]. Motivated by the observations of pulverized rocks along the San Andreas Fault zone near Tejon Pass, CA, USA [6,7,25,27], Doan & Gary [1] performed SHPB experiments on specimens of Tejon Lookout granite collected from just outside the heavily pulverized damage zone. They concluded that the transition from failure along a few discrete fracture planes to fragmentation occurs in Tejon Lookout granite beyond a critical strain rate threshold of approximately 150 s⁻¹. To study the effect that any pre-existing damage may have had on the tests, they conducted similar experiments on Tarn granite, a relatively undamaged rock, and found an increase in the critical strain rate of transition to fragmentation (approx. 250 s⁻¹). Doan & d'Hour [37] showed that the data agree with statistical theories for fracture propagation, wherein the rate-dependent brittle response of the material depends on the pre-existing flaw density and length distribution within the specimen. They suggest that pulverized rocks form via a feedback process, wherein a rock sustains cumulative profuse microcrack damage from each successive high strain rate loading event, which, in turn, reduces the strain rate threshold of fragmentation for the next event. Therefore, pulverized rocks may be considered a marker of repeated high strain rate loading events, a conclusion reinforced by subsequent work [38]. Experiments accounting for the effects of burial depth by encasing rock specimens in confinement collars have also shown that initially undamaged Westerly Granite consistently transitioned to fragmentation at strain rates of approximately 250 s⁻¹, and that this threshold increases with increasing confining pressure [2].

Correspondence between fast loading rate, strength/energy consumption increase and increase in fracture surface area created during SHPB tests has been recognized and documented qualitatively using optical and scanning electron microscopy (SEM) [4,5,39,40]. However, in the geologic literature, very few efforts to directly measure the energy partitioned into fracture growth during dynamic loading of rocks have been documented, and published data on the

degree of fragmentation in laboratory and natural settings are few. Moreover, the focus is often placed on the final wear product, without regard to differentiating fragments formed through distinct deformation mechanisms. Keulen *et al.* [8] suggested that grain size reduction in fault zones develops via two distinct mechanical processes: fragmentation is induced during initial rupture, and continued, lower strain rate comminution into gouge occurs through grinding wear and shear processes during subsequent slip. They argued that changes in the dominant mechanism of comminution are reflected in particle morphology and size distribution. High-speed friction experiments commonly yield nanoparticles [41] exhibiting a specific surface area (SSA) in one case of approximately $16\,\mathrm{m}^2\,\mathrm{g}^{-1}$ [22], although it is unclear how much of this grain size reduction is caused by mechanical fragmentation during the initial acceleration phase of slip versus abrasive wear or chemical reactions during shearing. Brunauer–Emmett–Teller (BET) surface area analysis of fresh gouge collected from a recently exposed shear fracture in quartzite with small net slip yielded an SSA of approximately $0.7\,\mathrm{m}^2\,\mathrm{g}^{-1}$ [24].

2. Material and methods

(a) Specimen selection and preparation

We focus on two rock types in this study: Arkansas Novaculite (AN) and Westerly Granite (WG). AN is a compositionally homogeneous, minimally porous (\ll 1%) and mechanically isotropic quartz rock, which is virtually flaw-free above the grain scale (5–10 µm for specimens used in this study; see §3b). As such, AN is an ideal analogue and well suited for evaluating continuum-based micromechanical models of brittle failure in rocks. WG is polymineralic (27% quartz, 66% feldspars, 5% micas and 2% accessory minerals [42]), coarser-grained (approx. 700 µm [43]) and mechanically isotropic at the hand-sample scale. It was selected as a well-studied counterpart that is more representative of the continental crust. Specimens were cored into cylinders and faces were machined perpendicular to the axial direction to a tolerance of 0.025 mm. In this study, we work with two specimen dimensions: $L/D \simeq 12$ mm/25 mm $\simeq 0.5$ and $L/D \simeq 15$ mm/15 mm $\simeq 1.0$, both within the recommended range of slenderness ratios [44].

(b) Experimental procedure

The SHPB consists of a loading apparatus and a system for monitoring mechanical response. The loading apparatus used in this study (figure 1) is composed of a compressed gas gun and three 38.1 mm diameter C-250 maraging steel bars (striker bar, incident bar and transmission bar; figure 1) of density $\rho_b = 8.054 \,\mathrm{g \, cm^{-3}}$ and Young's modulus $E_b = 185 \,\mathrm{GPa}$. The length of the incident and transmission bars is 2370 mm, and the striker bars are 229 and 305 mm long. Signals from two strategically placed metallic foil-type strain gauges sampling at a frequency of 125 MHz are treated by a signal conditioning amplifier and digitally recorded using a highspeed oscilloscope. The SHPB operates by firing the striker bar, the velocity of which is monitored with optical sensors located on the gun barrel. The striker impacts the incident bar, generating a compressive wave (incident pulse) that travels along the incident bar towards the cylindrical specimen sandwiched between the incident and transmission bars. Striker bar length controls the load duration experienced by the specimen, and varying the striker bar impact speed changes the loading rate and stress amplitude. Upon reaching the specimen, part of the wave energy (reflected pulse) is reflected from the incident bar/specimen interface back along the incident bar. The remaining wave energy (transmitted pulse) is transmitted through the specimen/transmission bar interface and absorbed by a bar stop at the end of the transmission bar. The strain gauges record the incident, reflected and transmitted waves, which Kolsky [45] showed can be related to the instantaneous stress, strain and strain rate in the specimen as long as dynamic force equilibrium is maintained on both of the specimen faces during loading. We employ pulseshaping materials at the impact end of the incident bar to satisfy the force equilibrium assumption (see the electronic supplementary material for details). In the SHPB configuration used in this

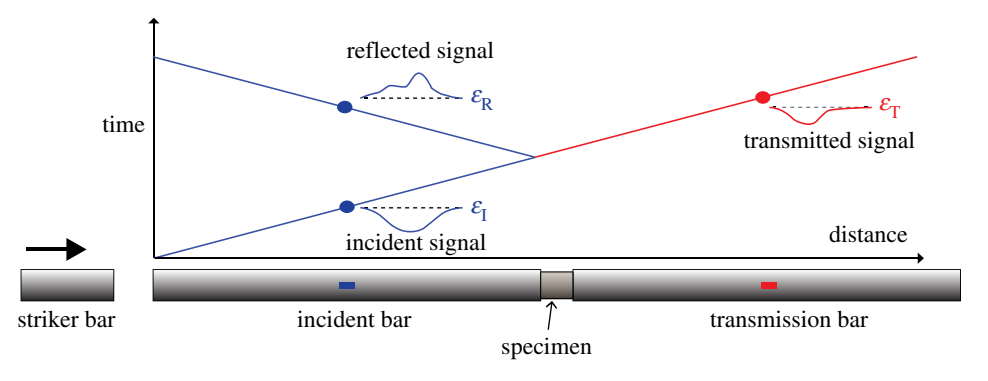


Figure 1. Conceptual diagram of a compressive SHPB system depicting the loading apparatus and associated wave travel time—distance plot. (Online version in colour.)

study, a momentum trap mounted on the incident bar prevents the sample from being loaded by multiple reflections of the incident wave, thereby limiting the sample to a single loading pulse.

(c) Energy budget

The energy carried by an elastic wave during an SHPB experiment can be represented as

$$W = \left(\frac{1}{2}\rho_{b}A_{b}C_{b}^{3} + \frac{1}{2}A_{b}C_{b}E_{b}\right)\int_{0}^{t} \varepsilon_{b}^{2}(t) dt, \tag{2.1}$$

where ρ_b is the density of the bar material, E_b is the bar Young's modulus, A_b is the bar cross-sectional area, C_b is the bar material elastic wave speed and $\varepsilon_b(t)$ is the instantaneous strain measured in the bar [46]. The total energy consumed in damaging the specimen, W_d , is

$$W_{\rm d} = W_{\rm I} - W_{\rm R} - W_{\rm T},\tag{2.2}$$

where W_I , W_R and W_T represent the energy carried by the incident, reflected and transmitted waves, respectively. The energy consumed in damaging the specimen can be further partitioned into energy used to create new fracture surfaces or *fracture surface energy*, W_f , and any other energy sinks in the system, W_o (e.g. kinetic energy of fragments, heat and plastic deformation). The fracture surface energy is related to the other work budget terms by

$$W_{\rm f} + W_{\rm 0} = W_{\rm d} = W_{\rm I} - W_{\rm R} - W_{\rm T}. \tag{2.3}$$

To characterize W_f , we examine select postmortem specimens by mechanical sieving, BET analysis of SSA (i.e. surface area per unit mass) and SEM.

(d) Postmortem damage characterization

All specimens are classified as intact, split/fragmented or intensely fragmented (figure 2) based on a qualitative characterization of damage state [1,2,47]. To characterize $W_{\rm f}$, we examine select postmortem specimens by mechanical sieving, BET analysis of SSA and SEM. To further explore the effect of comminution mechanism on fragment morphology and surface area, additional specimens were hand-ground and analysed using BET surface area measurements and SEM as well. Undamaged samples of AN and WG were sectioned into thin slivers using a low-speed diamond saw to minimize internal deformation. The resulting slivers were then slowly hand-ground using a steel mortar and pestle. To generate enough material in the smallest size fraction for gas adsorption analysis, hand-ground particles often underwent multiple cycles of sieving and grinding until sufficient fine material was generated. Because of the bias imparted by this

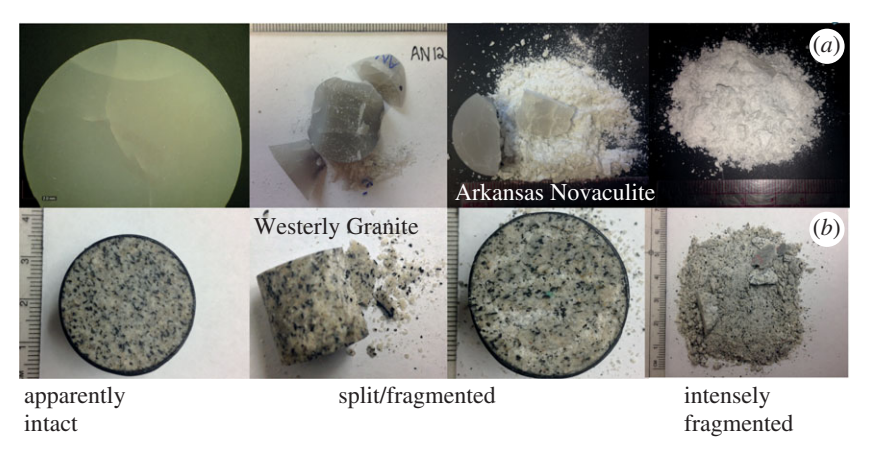


Figure 2. Qualitative classification of postmortem specimen damage for AN (a) and WG (b) tests. (Online version in colour.)

Table 1.	Particle size	and related in	nverse radius range.
----------	---------------	----------------	----------------------

particle size (mm)	inverse radius (mm ⁻¹)
2.0-1.0	1.0-2.0
1.0-0.5	2.0-4.0
0.5–0.25	4.0-8.0
0.25-0.125	8.0–15.9
0.125-0.063	15.9–31.7
0.063-0	>31.7

crushing procedure, no meaningful relationship should exist between the mass of each hand-ground size fraction and the initial mass of intact material. Thus, the particle size distribution (PSD) was not measured for hand-ground specimens. Sieving and gas adsorption were conducted on ground specimens according to the same procedure as the dynamically fragmented specimens.

Measurement of SSA using the BET gas adsorption method [48] considers the quantity of adsorbate gas molecules of effective surface area $A_{\rm m}$ adsorbed onto the accessible surfaces of an adsorbent material. Adsorbed gas is assumed to form a monolayer at very low pressure, and the adsorbed quantity is modelled as a function of gas pressure and temperature. For an ideal sphere of density ρ , geometric SSA, SSA_{ideal}, scales linearly with particle radius r as

$$SSA_{ideal} = 3(\rho r)^{-1}.$$
(2.4)

Introducing a roughness factor λ accounts for real deviations from ideal spherical geometry, where λ is typically defined as the ratio of surface area of a real particle to that of an ideal sphere. Considering that all real rocks contain internal flaws down to the nanometre scale, the true SSA must also include a term to describe the internal surface area of the particle, SSA_{int}, such that

$$SSA = 3\lambda(\rho r)^{-1} + SSA_{int}.$$
(2.5)

It is common practice to extrapolate linear fits to plots of SSA versus inverse particle size (r^{-1}) to yield estimates of SSA_{int} [49]. We follow this practice and plot SSA against r^{-1} , such that equation (2.5) plots as a straight line with slope proportional to the average surface roughness, λ , of the particles and vertical intercept equal to SSA_{int} (see §3b). Table 1 relates the particle size bins used during sieving to corresponding ranges of r^{-1} .

Another common practice is to estimate collective particle surface area using size distributions [6,7,50,51]. Popular tools used for measuring particle size, such as Coulter counters and mechanical sieves, tend to size particles according to their smallest dimension, but give no information on particle shape, leading to an underestimation of surface area. This necessitates the assumption of some representative surface roughness to bring about more accurate estimates of real particle surface area. Gas adsorption offers an advantage over estimates of new crack surface area based on simple particle size analysis in that gases can account directly for surface roughness and penetrate into cracks intersecting particle surfaces.

Select dynamically fragmented specimens (AN07, AN09, AN18, AN19; WG01) as well as hand-ground specimens were mechanically dry sieved for 2 min into size fractions bounded by 0.0, 0.063, 0.125, 0.250, 0.5, 1.0, 2.0 and greater than 2.0 mm. All subsamples were outgassed for 3 h at 200°C prior to analysis and the adsorptive gas used in this study was Kr. Scanning electron micrographs of specimen fragments from each size fraction were used to describe particle surface morphology and to further delineate PSDs beyond the resolution of sieve size bins. The BET measured SSA of the different size fractions for an individual specimen were measured and summed to yield the total particulate surface area for that specimen. Fracture surface area measurements are used to calculate equated estimates of the portion of energy dissipated in the creation of new surface area during a single loading event.

3. Results

(a) Mechanical results

Bringing the rock to failure at low strain rates posed a challenge due to the high uniaxial compressive strength (UCS) of AN. As such, very few specimens failed via localized, throughgoing fractures. Dynamic UCS of AN ranges from about 1.0– $1.3\,\mathrm{GPa}$ at strain rates of 130– $170\,\mathrm{s}^{-1}$ to about 1.65– $1.80\,\mathrm{GPa}$ at strain rates of 250– $580\,\mathrm{s}^{-1}$ (figures 3a and 4a). Dynamic UCS of WG (figures 3b and 4b) ranges from about 280 to $375\,\mathrm{MPa}$ at strain rates of 150 to $900\,\mathrm{s}^{-1}$. With the exception of one of the WG tests, the stress versus strain curve predicted the qualitative damage state for both AN and WG tests, with apparently intact specimens elastically unloading with a slope similar to that of the loading portion of the curve, split/fragmented specimens unloading but retaining permanent strain, and intensely fragmented specimens completely losing their load-bearing capacity (figure 3).

Previous studies using the SHPB to test brittle deformation of rocks have demonstrated that peak stress and strain rate delineate the transition to fragmentation [1,2,38]. While our tests on WG appear to follow that trend, the relationship between failure mode, peak stress and strain rate for our tests on AN appears less clear. While all intensely fragmented AN samples failed at stresses greater than $1600\,\mathrm{MPa}$ and strain rates greater than $400\,\mathrm{s^{-1}}$, several specimens that failed via discrete fracture did so at lower peak stresses and strain rates than other specimens which remained apparently intact (figure 4). Consistently, this occurred for tests with longer pulse duration. Conversely, intense fragmentation only occurred for pulse durations less than $160\,\mathrm{\mu s}$. For a complete summary of SHPB experimental conditions and mechanical results, see the electronic supplementary material, tables S1 and S2.

(b) Postmortem damage results

The PSDs of all the intensely fragmented AN specimens are comparable, as a first-order approximation. The mass majority of particles fall between 0.063 and 2.0 mm (figure 5). By contrast, the PSDs of intensely fragmented WG specimens are consistently positively skewed, showing a particularly larger mass percentage of particles greater than 2 mm. BET SSA measurements were performed on individual size fractions from a total of five (one handground and four dynamically fragmented) AN specimens and two (one hand-ground and one dynamically fragmented) WG specimens (figure 6).

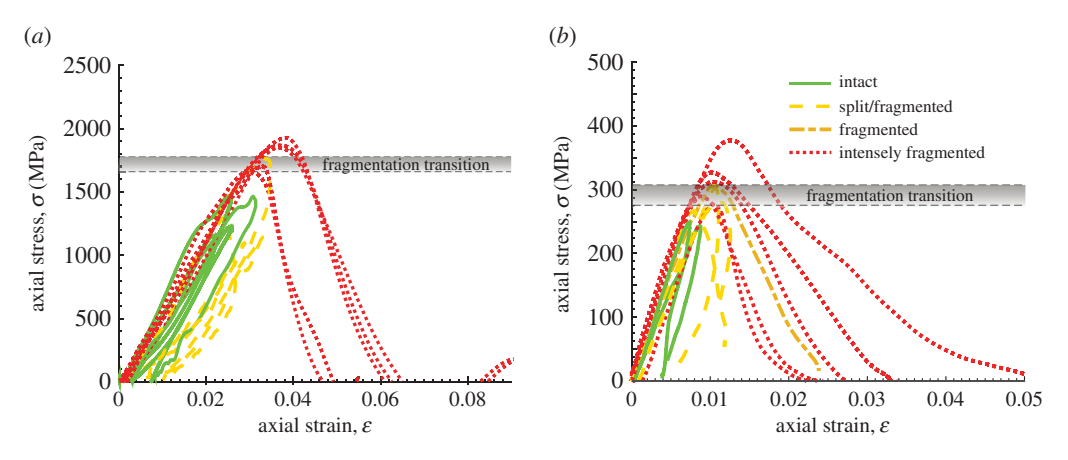


Figure 3. Axial stress versus axial strain curves for SHPB tests on (a) AN and (b) WG. Here the fragmentation transition marks the transition to intense fragmentation. Note that one WG specimen was classified as simply 'fragmented' (marked by the tan (light) coloured, dashed-dotted curve). This specimen fragmented into several large fragments, each of which contained pervasive microfracture, and the specimen lost all load-bearing capacity. We therefore interpret this specimen to best mark the end of transition to intense fragmentation in WG. See electronic supplementary material, figure S4, for sample IDs. (Online version in colour.)

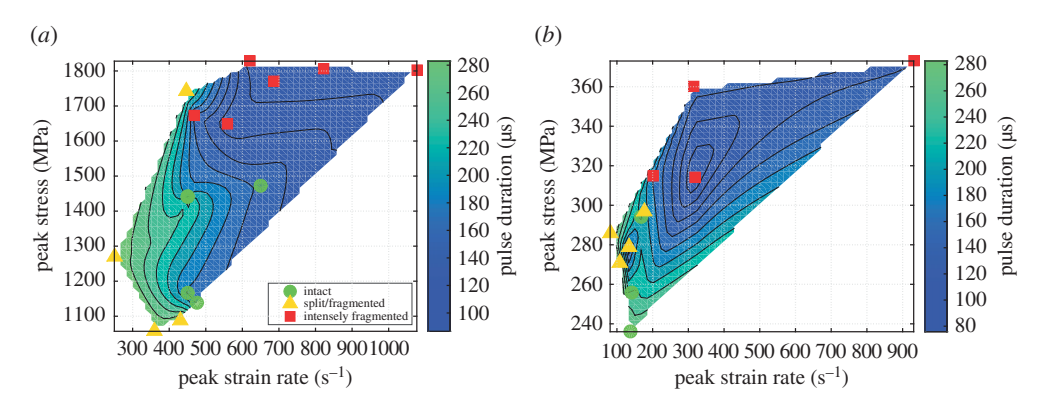


Figure 4. Peak stress versus peak strain rate experienced prior to failure shown with contours of incident pulse duration for (a) AN and (b) WG specimens loaded with the SHPB. Green circles, yellow triangles and red squares represent specimens classified as intact, split/fragmented and intensely fragmented, respectively. See the electronic supplementary material, tables S1 and S2, for sample IDs. (Online version in colour.)

The SSA of both pulverized and hand-ground AN (figure 6a) generally scale inversely with particle size. The values of SSA for different particle size bins range from 0.0453 to $0.7065\,\mathrm{m}^2\,\mathrm{g}^{-1}$ for dynamically fragmented AN and from 0.0363 to $0.1779\,\mathrm{m}^2\,\mathrm{g}^{-1}$ for the corresponding hand-ground material. These values are comparable to those reported by Olgaard & Brace [24] for BET surface area measurements made on fresh quartzite fault gouge collected along mining-induced shear fractures. The linear fit to dynamically fragmented samples is poor, particularly in the range $10\,\mathrm{mm}^{-1} < r^{-1} < 30\,\mathrm{mm}^{-1}$, where the scatter is large. The slope of the linear fit to dynamically fragmented specimens ($\lambda = 8.92$) is large relative to that of the hand-ground samples ($\lambda = 1.94$). As the model suggests, this might be interpreted as greater particle surface roughness, but also might be caused by a greater sub-fraction of fine (submicrometre particles) in the dynamically fragmented samples not delineated by the sieving process. For specimens AN18 and AN19, insufficient material in the less than $63\,\mathrm{\mu m}$ size range was collected to perform BET analysis. Therefore, only for specimens AN07 and AN09 could the surface area from each size

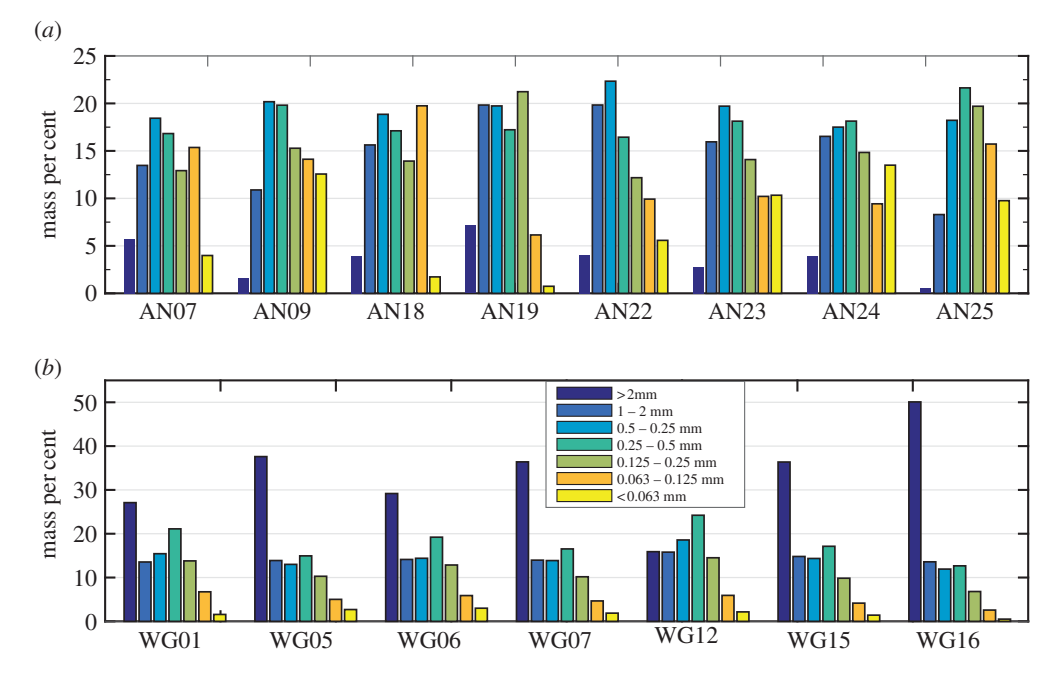


Figure 5. Histograms of PSD by mass per cent for dynamically fragmented specimens of (a) AN and (b) WG. (Online version in colour.)

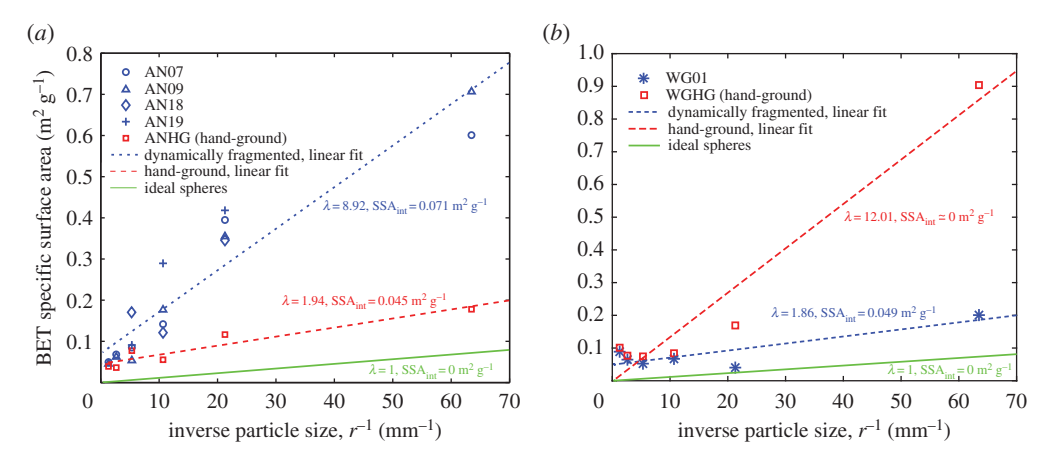


Figure 6. BET measured SSA plotted against the inverse of radius (r^{-1}) on different size fractions of (a) AN and (b) WG specimens. Blue (upper short dashed line and symbols) and red (lower dashed line and squares) data represent dynamically fragmented and hand-ground specimens, respectively. Linear fits to data are based on equation (2.5), with model parameters indicated adjacent to each curve. Green solid curve (bottom) represents geometric surface area of ideal spheres. (Online version in colour.)

fraction be summed to yield the total new fracture surface area created during the experiment. Some previous studies have presented fracture surface area in units of square metres per cubic metre of dynamically fragmented material = [m $^{-1}$] [8,30]. The weighted average SSA measured in experiments AN07 and AN09 was 0.217 and 0.320 m 2 g $^{-1}$, respectively, which is equivalent to 5.73×10^5 and 8.45×10^5 m $^{-1}$.

SSA trends in WG (figure 6b) show some key contrasts to trends in AN data. At smaller r^{-1} values (larger particle sizes), both dynamically fragmented and hand-ground WG specimens

Table 2. Summary of fracture surface energy analysis.

sample ID	sample mass (g)	% mass collected	average BET SSA (m² g ^{—1})	total SA (m²)	fractal dim., <i>D</i> f	W ₁ (J)	<i>W</i> _d (J)	<i>W</i> _f (J)	$W_{\rm f}/W_{ m d}$
AN07	15.38	87.26	2.90-5.65	44.6-86.9	3.14	1461	433	44.6-86.9	0.10-0.20
AN09	15.26	82.36	4.02-7.83	61.3-119.5	2.83	1186	268	61.3-119.5	0.22-0.45
WG01	15.76	98.41	0.076	1.90	2.65	215	51	1.90	0.04

show similar SSA values, which decrease with r^{-1} up to a point delineated by the $r^{-1} = 3.0 - 4.0\,\mathrm{mm}^{-1}$ inverse particle size, which corresponds closely with the mean grain size of WG (approx. 750 µm). Beyond this delineation (i.e. at smaller particle sizes), SSAs of dynamically fragmented and hand-ground granite specimens generally increase with r^{-1} , but deviate from one another significantly (by a factor of 8 at the smallest particle size range), suggesting a fundamental difference between hand-ground and dynamically fragmented granite specimens below a threshold particle size. SSA for different particle size bins ranged from 0.0526 to 0.201 m² g⁻¹ for dynamically fragmented WG and from 0.0730 to 0.904 m² g⁻¹ for the corresponding hand-ground material. The weighted average SSA measured in experiment WG01 was 0.0762 m² g⁻¹, equivalent to 2.02×10^5 m⁻¹.

Table 2 summarizes the fracture surface energy analysis for specimens AN07, AN09 and WG01. Assuming a specific surface energy of 1 J m⁻² for quartz [52], we used dynamically fragmented specimen SSA to calculate the energy dissipated in brittle fracture, W_f , during a single loading event. When a rock fails via dynamic fragmentation, the resulting fragments explode outward with substantial kinetic energy and capturing all of the particles proves difficult, especially for the smallest particles generated, which are powders. For tests on WG, between 98 and 99% of the original specimen mass was collected. However, for tests on AN, which generates substantial amounts of fine particles upon fragmentation, capture efficiency was between 82 and 94%. In our analysis under the SEM, the smallest identifiable particles fell in the range of 0.5–1.0 µm. If we consider that the lost particles were as fine as or finer than the smallest fragments observed, we can extrapolate the linear fit for the dynamically fragmented data in figure 6a out to r^{-1} values equivalent to particle diameters of 1.0 and 0.5 μ m. These calculations indicate that AN specimens dissipated a substantially larger portion of energy (10-40%) in creating new fracture surface area than WG (approx. 5%), owing to the significant contribution of the finest particles. Table 2 also summarizes the computed fractal dimension, D_f , of particles for the same three specimens (see the electronic supplementary material for details). The fractal dimension $(2.65 \le D_f \le 3.14)$; table 2) of our dynamically fragmented particles is comparable to that reported by Keulen et al. [8] for 'cracked grains' or particles that the authors associated with dynamic fragmentation during coseismic deformation.

Direct microstructural observations of the postmortem specimens yield some important insights into the micromechanical processes responsible for fragmentation, and how these processes vary with loading rate, loading configuration and lithology. In AN, microcracking occurs well below the fragmentation threshold, and, indeed, well below the macroscopic strength of the rock (figure 7b). In these cases, cracks are opening mode and align with the direction of the axial load. For specimens dynamically fragmented using the SHPB, individual fragments span several orders of magnitude in size, but abundant submicrometre particles are produced, far below the grain size of undeformed AN, attesting to the importance of intragranular fracturing in addition to fracture along grain boundaries (figure 7c,d). In some cases, intergranular fractures cut across otherwise undeformed grains (figure 7e,f). Fragment surfaces are characterized by conchoidal fracture and twist hackle (figure 7f), and partially coated by submicrometre particles. The predominance of this texture attests to the important role of mixed mode I–III fracture propagation [53], probably due to interaction between adjacent propagating microcracks as

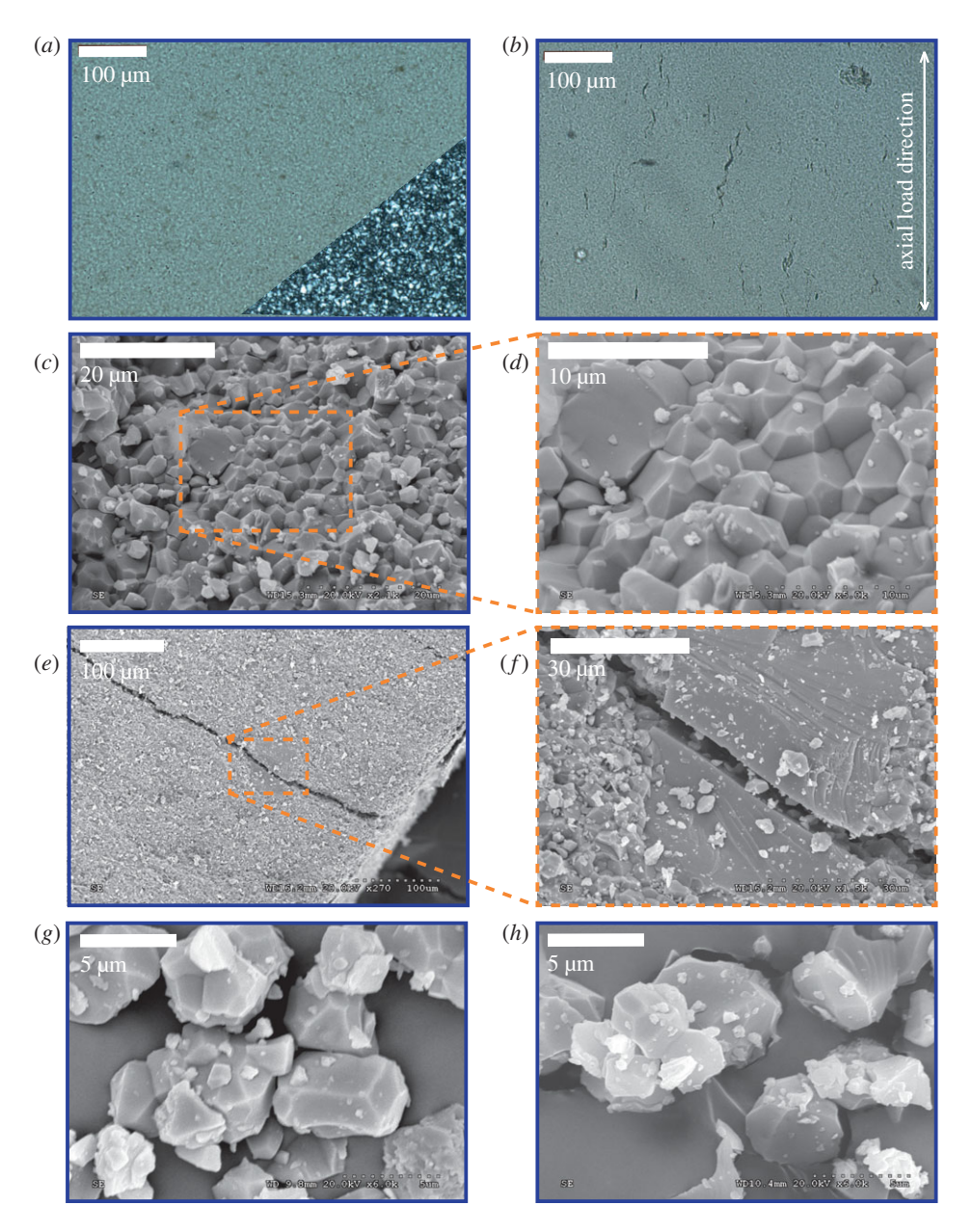


Figure 7. Optical light and SEM images of AN specimens. (a) Plane polarized light (PPL) image of undeformed AN showing the absence of flaws above the 5–10 μ m grain scale (grains highlighted by crossed polarized light (CPL) corner inset). (b) PPL image of apparently intact postmortem specimen (AN02) after the SHPB test showing dynamically grown microcracks parallel to the axial stress direction. (c,d) Surface of a dynamically fragmented (AN07) particle showing intra- and intergranular cracking features. (e,f) Surface of a larger (1–2 mm) fragment from AN07 showing abnormally large grain cut by intergranular fracture with twist hackle surface texture. (g,h) Equant grain-scale particles resulting from (g) dynamic fragmentation (AN24) and (g) hand-grinding (WG HG). (Online version in colour.)

the sample approaches the intense fragmentation state. The smallest abundant particle size for both dynamically fragmented and hand-ground AN is approximately $3-10\,\mu\text{m}$, each particle corresponding to individual quartz grains, and submicrometre particles appear present in roughly the same amounts (figure 7g,h).

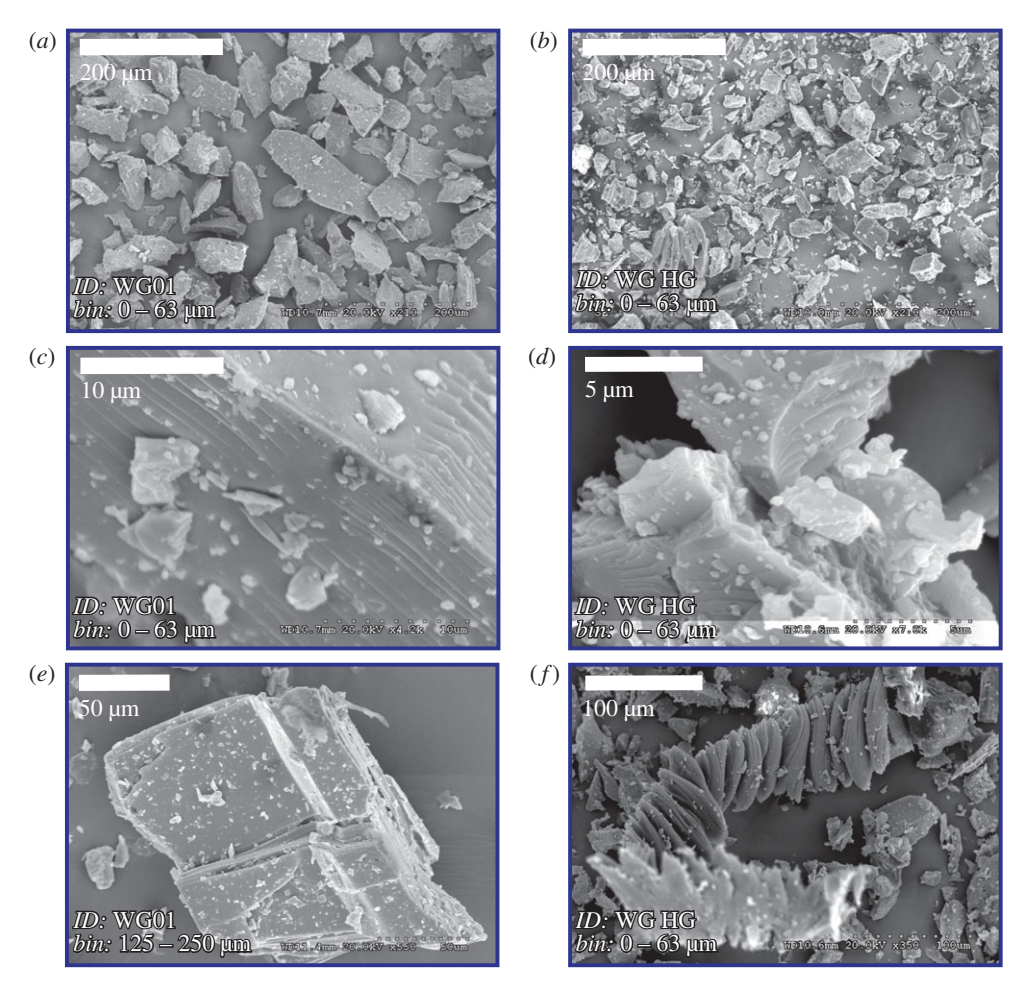


Figure 8. SEM images of deformed WG specimens. (a,b) Fragments from smallest sieve size bin (less than 63 μ m) are substantially larger for (a) dynamically fragmented granite (WG01) than for (b) the corresponding hand-ground specimen (WG HG). (c,d) Fracture surfaces exhibiting twist hackle and coated with submicrometre particles on fragments of both (c) dynamically fragmented (WG01) and (d) hand-ground (WG HG) granite specimens. (e,f) Mica grains showing (e) substantial surface exposure manifested as opening along grain boundaries and cleavage planes in WG01 and (f) extraordinary shearing along cleavage planes in hand-ground WG HG. (Online version in colour.)

Postmortem specimens of dynamically fragmented and hand-ground WG display some key differences compared to AN. In general, individual particles are less equant than AN, perhaps owing to the heterogeneous mineralogy, as the long dimension of individual particles is frequently parallel to an obvious cleavage plane in biotite and feldspar fragments (figure 8a,e). Quartz grains in both dynamically fragmented and crushed samples display common joint surface textures, particularly twist hackle, on particles ranging in size from a few to hundreds of micrometres (figure 8c,d). In dynamically fragmented and hand-ground specimens, equant submicrometre particles coat larger fragments, yet submicrometre-sized particles appear, qualitatively, to be far more prevalent in hand-ground granite samples (figure 8d) than in hand-crushed AN. The hand-ground and, to a lesser degree, the dynamically fragmented WG specimens show abundant evidence of shear deformation on cleavage planes (figure 8e,), most dramatically displayed by smeared biotite grains (figure 8f), and the average particle in the smallest size fraction bin (less than $63 \, \mu m$) is substantially smaller for the hand-ground (figure 8b) than for the dynamically fragmented (figure 8a) WG sample.

4. Discussion

(a) Fracturing as a component of dissipated energy

Taken together, the mechanical data from SHPB experiments, as well as BET SSA data and microstructural observations, provide important insights into the role of material heterogeneity and anisotropy on the fragmentation process under compressive loading. The data spread, and resulting nonlinear character of the SSA versus r^{-1} relationship for AN, particularly in the inverse particle size range of $10 \,\mathrm{mm}^{-1} < r^{-1} < 30 \,\mathrm{mm}^{-1}$ (figure 6a), is likely a product of the adherence of abundant submicrometre-sized particles to larger particles (figure $7d_f$). Conversely, the nonlinearity in the SSA versus r^{-1} relationship in WG is characterized by a non-intuitive decrease in SSA with increasing r^{-1} in the range $0 \,\mathrm{mm}^{-1} < r^{-1} < 5 \,\mathrm{mm}^{-1}$ before increasing with r^{-1} (i.e. with decreasing particle size). It is noteworthy that the average grain diameter of 0.75 mm in WG $(r^{-1} \simeq 2.7 \,\mathrm{mm}^{-1})$ roughly delineates the change in dependence. The pervasive failure along cleavage planes in micas and feldspars (figure 8b,e,f) exposes new surfaces, whereas this effect is probably undersampled at successively smaller grain size fractions (increasing r^{-1}) up to the average grain size of the rock. This interpretation is supported by the fact that this trend is repeated for hand-crushed WG samples where shearing along cleavage planes is especially pervasive (figure 8f). Furthermore, the relatively high SSA measurements in the smallest size fraction from hand-ground specimens may be explained by a more finely skewed PSD within this size fraction bin (figure 8b), which is perhaps dominantly generated by the strong activation of shear deformation (figure 8f) driven by the grinding motion, but facilitated by the natural strength anisotropy of biotite and feldspar minerals. Such shear motion could enhance particle size reduction by wear and localized deformation at the tips of shear cracks, and no such pervasive evidence of shear deformation was observed in either the dynamically fragmented or hand-crushed AN samples.

The implied fracture energy associated with the SSA measurements is complicated by a number of factors. First, for experiments AN07 and AN09 (and to a lesser extent WG01), a nonnegligible amount of powder was lost, due primarily to escape of fine-sized particulate matter during the experiments; therefore, it is difficult to determine with great certainty the SSA of the missing size fraction. One approach to estimating this missing size fraction is to assume that the smallest size particles observed in the SEM are representative of the lost particles. If, for example, we assume a range of particle sizes of 0.5–1 μ m for AN09, this yields W_f/W_d of 20–40%. The WG specimens are more complicated. First, the measured SSA is smaller for dynamically fragmented WG compared to slowly hand-crushed WG, but the total dissipated energy was also smaller, so W_f/W_d is similar to the AN samples. The relatively minor mass percentage of fine (i.e. less than 63 µm) particles in the dynamically fragmented WG samples suggests that the real surface area of the particles may be significantly smaller than those produced during AN experiments. Furthermore, owing to the activation of shear on anisotropic grains in WG, it is more difficult to ascribe all of the measured surface area to fracture energy. Instead, shearing on pre-existing planes of weakness is likely to result in a greater portion of energy dissipated into heat.

It is also worth noting that these results show that uniaxial compression at fast strain rates can produce submicrometre particles. This observation suggests that the quasi-static model of a 'grind limit' [35] may be a reasonable idealization for slow deformation rates, but that, in the strain rate spectrum of the SHPB (and near the earthquake rupture tip), it is no longer valid.

These experimental observations produce an interesting point of comparison to the theoretical predictions of coseismic temperature rise due to distributed fracture and fragmentation in a fault damage zone [54]. Based on stress–strain curves obtained from SHPB experiments on WG under confinement [2], Ben-Zion & Sammis [54] estimated the dissipated strain energy available for fragmentation and shear heating. Calculating the total surface area created by reducing the original rock volume into $1\,\mu\text{m}^2$ cubes resulted in an SSA of $2\,g\,\text{m}^{-2}$, and the percentage of total work consumed by creation of new fracture surface was small compared to the total dissipated

energy; they therefore concluded that nearly all of the dissipated energy goes into shear heating. Our SSA data, which produce roughness constants of $\lambda \approx 9$ for AN and $\lambda \approx 2$ for WG, result in an SSA of approximately $1\,\mathrm{g\,m^{-2}}$, remarkably like the simple thought experiment of Ben-Zion & Sammis [54]. However, given the error introduced to our measurements by the missing abundance of submicrometre particles, we have shown that the total work invested in fracture may be as great as 40% for AN. Therefore, we may conclude that, in relatively homogeneous and undamaged crystalline rocks, temperature rise might be buffered by the creation of fractures, whereas in heterogeneous and heavily pre-fractured media, the majority of dissipated energy would be converted to heat.

(b) Implications for faulting, friction and weakening

This study represents the first quantitative investigation of the amount of dissipated energy partitioned into fracture energy during impulsive compressive loading events on initially intact rocks. And while we cannot yet robustly predict the relationship between loading parameters and fracture surface area created, our observations provide a number of insights relevant to the role of pulverization in the seismic faulting process.

In particular, it suggests that, for several tens of centimetres near the fault where stresses and strain rates exceed dynamic fragmentation thresholds for common crustal rocks under uniaxial compression, rock fragmentation can be an effective energy sink to account for a significant portion of dissipated energy, providing a mechanism for the energy sink hypothesized by Nielsen *et al.* [31]. As an example, consider a volume of rock surrounding the psz that is pulverized during an approximately M6 earthquake. Taking $W_f = 100 \, \mathrm{J}$ as an upper bound on our results for 15 g specimens of AN (table 2), of mass density $d = 2700 \, \mathrm{kg \, m^{-3}}$, yields an energy density of 18 MJ per cubic metre of pulverized rock. If a thickness of 10 cm is pulverized, the total work dissipated is 1.8 MJ m⁻² of fault area, a substantial portion of the total energy lost in breakdown work or 'fracture energy' as reported for high-speed friction tests (approx. 1–3 MJ m⁻² for slip greater than 1 m; fig. 5 of [31]) and a significant portion of that reported for large natural earthquakes (approx. 1–18 MJ m⁻² [55]).

Our results also suggest that the values of W_f may represent an upper bound for crystalline rocks. The differences between surface area measurements and microstructural observations of AN and WG suggest that homogeneous continuum models may overestimate the role of mode I fracturing in the fragmentation process, and that shearing on pre-existing weak planes may play a larger role. We view the observations in WG as a microscale analogue for activation of small damage zone faults and fractures along mature faults [17,54,55]. Intense fracture and/or pulverized rocks are likely the end result of inelastic yielding in the process zone of a propagating rupture, but the extent and actual micromechanisms responsible might depend on the degree of heterogeneity and existing damage within the damage zone. Furthermore, one might conjecture that, depending on the mode of damage (cracking versus shearing), the dissipated energy might be variably partitioned into distributed heat, or creation of new fracture surface. Our results indicate that loading conditions relevant to the tip of a propagating earthquake rupture are an effective mechanism for initiating grain size reduction, and, as these generally correspond to the particle acceleration phase of a passing rupture [23], this grain size reduction may kick-start rapid weakening due to initial grain size reduction and the exposure of fresh particle surfaces, optimizing the activation of subsequent physicochemical weakening processes [56]. Our estimates of SSA in dynamically fragmented specimens are an order of magnitude smaller than similar measurements performed on experimentally produced gouge by Reches & Lockner [22]. Based on our experimental results, initial grain size reduction at the tip of a rupture may form the initial stages of weakening, partially confirming the hypothesis of Reches & Dewers [12], but wear processes are necessary to continue the grain size reduction to the extent of that observed in gouge material on some mature faults [6,9,26].

(c) Open questions

All of the foregoing discussion points are subject to the limitation that the applied loads in the SHPB experiments in this study all consist of smoothly shaped, uniaxial compressive loads with a single cycle of deformation. This results in a scaling challenge on a number of fronts. First, the loading history (including the duration of the applied load) is essential to predicting the brittle yielding behaviour. The peak or average stress and strain rate alone do not provide enough information. This conclusion is supported by a recent study which showed that repeated loading cycles at peak stresses and strain rates below the dynamic fragmentation transition lower the corresponding thresholds for fragmentation in rocks [38]. Furthermore, the load history applied to a rock during passage of a dynamic rupture is subject to rapid cycles of loading, which, depending on the position relative to the fault (and other complicating factors, e.g. [54]), may vary in amplitude, duration and orientation, and also may combine transient pulses of tension and compression [12,56]. Therefore, in order to constrain the constitutive inelastic yielding behaviour of rocks due to impulsive loads relevant to earthquake ruptures, future work will need to focus on replicating these more realistic load histories.

5. Conclusion

We conducted a series of dynamic compression tests on weakly confined AN and WG. The dynamic fragmentation thresholds for WG, as defined in terms of stress and strain rate, were similar to those found in previous work on unconfined or weakly confined samples [2]. Dynamic fragmentation thresholds for AN, however, are much higher ($\sigma \approx 1600 \,\mathrm{MPa}$ and $\dot{\varepsilon} \approx 400 \,\mathrm{s}^{-1}$), but the yield strength at slightly lower strain rates is highly dependent on load duration. PSDs indicate that a larger percentage of WG rock mass is converted to large fragments, compared to AN. SSA measurements suggest that more of the available energy is invested into creating new fracture surface for AN. Furthermore, dynamic fragmentation of AN produces more SSA than the slower process of mechanical grinding, whereas the opposite is true for WG. Microstructural observations indicate that submicrometre particles are produced in varying amounts for the different experiments, and that mode I cracking, including intergranular fracture, is the dominant grain size reduction in fragmentation of AN, whereas exploitation of cleavage planes and minor shearing are also important in WG. Furthermore, SSA measurements for AN, corrected for missing submicrometre particles, suggest that up to 40% of dissipated energy in the experiments is invested in the creation of new fracture surfaces, and that pulverization may represent a substantial portion of the fracture energy observed during large earthquakes. This implies that dynamic fragmentation can be a significant sink for earthquake energy, and that grain size reduction by compressive stress waves at the earthquake rupture tip can dynamically weaken faults.

Data accessibility. This article has no additional data.

Competing interests. We declare we have no competing interests.

Funding. T.B. was supported by the National Science Foundation Graduate Research Fellowship under grant no. 1144240. Research was sponsored by the Army Research Laboratory under grant no. W911NF-14-1-0276 and the National Science Foundation under NSF-EAR Award (1351931).

Acknowledgements. We thank Stefan Nielsen and two anonymous reviewers, whose generous, constructive feedback improved the quality of the final manuscript. This study benefited greatly from discussions with Hamed Ghaffari, Chris Borjas and Qinhong Hu. We acknowledge Kermit Beird and Merlynd Nestell for their contributions in specimen preparation, as well as Jiechao Jiang, Majie Fan, Elizabeth Griffith and Samantha Carter for help with microstructural analysis.

Disclaimer. The views and conclusions contained in this document are those of the authors and should not be interpreted as representing the official policies, either expressed or implied, of the Army Research Laboratory or the U.S. Government. The U.S. Government is authorized to reproduce and distribute reprints for Government purposes notwithstanding any copyright notation herein.

References

- 1. Doan M-L, Gary G. 2009 Rock pulverization at high strain rate near the San Andreas fault. *Nat. Geosci.* **2**, 709–712. (doi:10.1038/ngeo640)
- 2. Yuan F, Prakash V, Tullis T. 2011 Origin of pulverized rocks during earthquake fault rupture. *J. Geophys. Res. Solid Earth* **116**, 1–18. (doi:10.1029/2010JB007721)
- 3. Xia K, Yao W. 2015 Dynamic rock tests using split Hopkinson (Kolsky) bar system a review. *J. Rock Mech. Geotech. Eng.* **7**, 27–59. (doi:10.1016/j.jrmge.2014.07.008)
- 4. Ravi-Chandar K, Yang B. 1997 On the role of microcracks in the dynamic fracture of brittle materials. *J. Mech. Phys. Solids* 45, 535–563. (doi:10.1016/S0022-5096(96)00096-8)
- 5. Zhang ZX, Kou SQ, Yu J, Yu Y, Jiang LG, Lindqvist PA. 1999 Effects of loading rate on rock fracture. *Int. J. Rock Mech. Min. Sci.* 36, 597–611. (doi:10.1016/S0148-9062(99)00031-5)
- 6. Wilson B, Dewers T, Reches Z, Brune J. 2005 Particle size and energetics of gouge from earthquake rupture zones. *Nature* **434**, 749–752. (doi:10.1038/nature03433)
- Rockwell T, Sisk M, Girty G, Dor O, Wechsler N, Ben-Zion Y. 2009 Chemical and physical characteristics of pulverized Tejon Lookout granite adjacent to the San Andreas and Garlock faults: implications for earthquake physics. *Pure Appl. Geophys.* 166, 1725–1746. (doi:10.1007/s00024-009-0514-1)
- 8. Keulen N, Heilbronner R, Stünitz H, Boullier A-MM, Ito H. 2007 Grain size distributions of fault rocks: a comparison between experimentally and naturally deformed granitoids. *J. Struct. Geol.* **29**, 1282–1300. (doi:10.1016/j.jsg.2007.04.003)
- 9. Mitchell TM, Ben-Zion Y, Shimamoto T. 2011 Pulverized fault rocks and damage asymmetry along the Arima–Takatsuki Tectonic Line, Japan. *Earth Planet. Sci. Lett.* **308**, 284–297. (doi:10.1016/j.epsl.2011.04.023)
- 10. Rempe M, Mitchell T, Renner JJ, Nippress S, Ben-Zion Y, Rockwell T. 2013 Damage and seismic velocity structure of pulverized rocks near the San Andreas Fault. *J. Geophys. Res. Solid Earth* **118**, 2813–2831. (doi:10.1002/jgrb.50184)
- 11. Fondriest M, Aretusini S, Di Toro G, Smith SAF. 2015 Fracturing and rock pulverization along an exhumed seismogenic fault zone in dolostones: the Foiana Fault Zone (Southern Alps, Italy). *Tectonophysics* **654**, 56–74. (doi:10.1016/j.tecto.2015.04.015)
- 12. Reches Z, Dewers TA. 2005 Gouge formation by dynamic pulverization during earthquake rupture. *Earth Planet. Sci. Lett.* **235**, 361–374. (doi:10.1016/j.epsl.2005.04.009)
- 13. Savage HM, Brodsky EE. 2011 Collateral damage: evolution with displacement of fracture distribution and secondary fault strands in fault damage zones. *J. Geophys. Res.* **116**, B03405. (doi:10.1029/2010]B007665)
- 14. Davatzes NC, Aydin A. 2005 Distribution and nature of fault architecture in a layered sandstone and shale sequence: an example from the Moab fault, Utah. In *Faults, fluid flow, and petroleum traps*, AAPG Memoir 85 (eds R Sorkhabi, Y Tsuji), pp. 153–180. Tulsa, OK: American Association of Petroleum Geologists. See https://pubs.er.usgs.gov/publication/70027340.
- 15. Delaney PT, Pollard DD, Ziony JI, McKee EH. 1986 Field relations between dikes and joints: emplacement processes and paleostress analysis. *J. Geophys. Res.* **91**, 4920. (doi:10.1029/JB091iB05p04920)
- 16. Vermilye JM, Scholz CH. 1998 The process zone: a microstructural view of fault growth. *J. Geophys. Res.* **103**, 12 223–12 237. (doi:10.1029/98JB00957)
- 17. Savage HM, Cooke ML. 2010 Unlocking the effects of friction on fault damage zones. *J. Struct. Geol.* **32**, 1732–1741. (doi:10.1016/j.jsg.2009.08.014)
- 18. Chester FM, Chester JS. 2000 Stress and deformation along wavy frictional faults. *J. Geophys. Res.* **105**, 23 421–23 430. (doi:10.1029/2000JB900241)
- 19. Griffith WA, Nielsen S, Di Toro G, Smith SAF. 2010 Rough faults, distributed weakening, and off-fault deformation. *J. Geophys. Res.* **115**, B08409. (doi:10.1029/2009]B006925)
- Griffith WA, Rosakis A, Pollard DD, Ko CW. 2009 Dynamic rupture experiments elucidate tensile crack development during propagating earthquake ruptures. *Geology* 37, 795–798. (doi:10.1130/G30064A.1)
- 21. Ngo D, Huang Y, Rosakis A, Griffith WA, Pollard D. 2012 Off-fault tensile cracks: a link between geological fault observations, lab experiments, and dynamic rupture models. *J. Geophys. Res. Solid Earth* **117**, B01307. (doi:10.1029/2011JB008577)
- 22. Reches Z, Lockner DA. 2010 Fault weakening and earthquake instability by powder lubrication. *Nature* **467**, 452–455. (doi:10.1038/nature09348)

- 23. Chang JC, Lockner DA, Reches Z. 2012 Rapid acceleration leads to rapid weakening in earthquake-like laboratory experiments. *Science* 338, 101–105. (doi:10.1126/science. 1221195)
- 24. Olgaard DL, Brace WF. 1983 The microstructure of gouge from a mining-induced seismic shear zone. *Int. J. Rock Mech. Min. Sci. Geomech. Abstr.* **20**, 11–19. (doi:10.1016/0148-9062(83) 91610-8)
- 25. Dor O, Ben-Zion Y, Rockwell TK, Brune J. 2006 Pulverized rocks in the Mojave section of the San Andreas Fault Zone. *Earth Planet. Sci. Lett.* **245**, 642–654. (doi:10.1016/j.epsl.2006.03.034)
- 26. Chester JS, Chester FM, Kronenberg AK. 2005 Fracture surface energy of the Punchbowl fault, San Andreas system. *Nature* **437**, 133–136. (doi:10.1038/nature03942)
- 27. Dor O, Rockwell TK, Ben-Zion Y. 2006 Geological observations of damage asymmetry in the structure of the San Jacinto, San Andreas and Punchbowl Faults in Southern California: a possible indicator for preferred rupture propagation direction. *Pure Appl. Geophys.* **163**, 301–349. (doi:10.1007/s00024-005-0023-9)
- 28. Dor O, Yildirim C, Rockwell TK, Ben-Zion Y, Emre O, Sisk M, Duman TY. 2008 Geological and geomorphologic asymmetry across the rupture zones of the 1943 and 1944 earthquakes on the North Anatolian Fault: possible signals for preferred earthquake propagation direction. *Geophys. J. Int.* **173**, 483–504. (doi:10.1111/j.1365-246X.2008.03709.x)
- 29. Ben-Zion Y, Shi Z. 2005 Dynamic rupture on a material interface with spontaneous generation of plastic strain in the bulk. *Earth Planet. Sci. Lett.* **236**, 486–496. (doi:10.1016/j.epsl.2005. 03.025)
- 30. Wechsler N, Allen EE, Rockwell TK, Girty G, Chester JS, Ben-Zion Y. 2011 Characterization of pulverized granitoids in a shallow core along the San Andreas Fault, Littlerock, CA. *Geophys. J. Int.* 186, 401–417. (doi:10.1111/j.1365-246X.2011.05059.x)
- 31. Nielsen S, Spagnuolo E, Violay M, Smith S, Di Toro G. 2016 G: fracture energy, friction and dissipation in earthquakes. *J. Seismol.* 20, 1187–1205. (doi:10.1007/s10950-016-9560-1)
- 32. Andrews DJ. 2005 Rupture dynamics with energy loss outside the slip zone. *J. Geophys. Res. B Solid Earth* **110**, 1–14. (doi:10.1029/2004JB003191)
- 33. Prasher CL. 1987 Crushing and grinding process handbook. New York, NY: Wiley.
- 34. Kendall K. 1979 The impossibility of comminuting small particles by compression. *Nature* **279**, 169–170. (doi:10.1038/279169d0)
- 35. Sammis CG, Ben-Zion Y. 2008 Mechanics of grain-size reduction in fault zones. *J. Geophys. Res.* **113**, B02306. (doi:10.1029/2006]B004892)
- 36. Rowe CD, Griffith WA. 2015 Do faults preserve a record of seismic slip: a second opinion. *J. Struct. Geol.* **78**, 1–26. (doi:10.1016/j.jsg.2015.06.006)
- 37. Doan ML, d'Hour V. 2012 Effect of initial damage on rock pulverization along faults. *J. Struct. Geol.* 45, 113–124. (doi:10.1016/j.jsg.2012.05.006)
- 38. Aben FM, Doan M-L, Mitchell TM, Toussaint R, Reuschlé T, Fondriest M, Gratier J-P, Renard F. 2016 Dynamic fracturing by successive coseismic loadings leads to pulverization in active fault zones. *J. Geophys. Res. Solid Earth* **121**, 2338–2360. (doi:10.1002/2015JB012542)
- 39. Lundberg B. 1976 A split Hopkinson bar study of energy absorption in dynamic rock fragmentation. *Int. J. Rock Mech. Min. Sci. Geomech. Abstr.* **13**, 187–197. (doi:10.1016/0148-9062(76)91285-7)
- 40. Xia K, Nasseri MHB, Mohanty B, Lu F, Chen R, Luo SN. 2008 Effects of microstructures on dynamic compression of Barre granite. *Int. J. Rock Mech. Min. Sci.* **45**, 879–887. (doi:10.1016/j.ijrmms.2007.09.013)
- 41. Han R, Shimamoto T, Hirose T, Ree J-H, Ando J-I. 2007 Ultralow friction of carbonate faults caused by thermal decomposition. *Science* **316**, 878–881. (doi:10.1126/science.1139763)
- 42. Brace WF, Martin RJ, Ladanyi B. 1970 A test of the law of effective stress for crystalline rocks of low porosity. *Int. J. Rock Mech. Min. Sci.* 7, 123–124. (doi:10.1016/0148-9062(70)90030-6)
- 43. Chen Y, Watanabe K, Kusuda H, Kusaka E, Mabuchi M. 2011 Crack growth in Westerly granite during a cyclic loading test. *Eng. Geol.* **117**, 189–197. (doi:10.1016/j.enggeo.2010.10.017)
- 44. Dai F, Huang S, Xia K, Tan Z. 2010 Some fundamental issues in dynamic compression and tension tests of rocks using split Hopkinson pressure bar. *Rock Mech. Rock Eng.* **43**, 657–666. (doi:10.1007/s00603-010-0091-8)
- 45. Kolsky H. 1949 An investigation of the mechanical properties of materials at very high rates of loading. *Proc. Phys. Soc. Sect. B* **62**, 676–700. (doi:10.1088/0370-1301/62/11/302)

- 46. Chen WW, Song B. 2011 Split Hopkinson (Kolsky) bar: design, testing and applications, Mechanical Engineering Series. New York, NY: Springer. (doi:10.1007/978-1-4419-7982-7)
- 47. Doan M-L, Billi A. 2011 High strain rate damage of Carrara marble. *Geophys. Res. Lett.* 38, L19302. (doi:10.1029/2011GL049169)
- 48. Brunauer S, Emmett PH, Teller E. 1938 Adsorption of gases in multimolecular layers. *J. Am. Chem. Soc.* **60**, 309–319. (doi:10.1021/ja01269a023)
- 49. Brantley SL, Mellott NP. 1998 Surface area and porosity of primary silicate minerals. *Am. Mineral.* **62A**, 229–230. (doi:10.1180/minmag.1998.62A.1.121)
- 50. Muto J, Nakatani T, Nishikawa O, Nagahama H. 2015 Fractal particle size distribution of pulverized fault rocks as a function of distance from the fault core. *Geophys. Res. Lett.* 42, 3811–3819. (doi:10.1002/2015GL064026)
- 51. Yoshioka N. 1986 Fracture energy and the variation of gouge and surface roughness during frictional sliding of rocks. *J. Phys. Earth* **34**, 335–355. (doi:10.4294/jpe1952.34.335)
- 52. Brace WF, Walsh JB. 1962 Some direct measurements of the surface energy of quartz and orthoclase. *Am. Mineral.* 47, 1111–1122. See http://www.minsocam.org/ammin/AM47/AM47_1111.pdf.
- 53. Pollard DD, Segall P, Delaney PT. 1982 Formation and interpretation of dilatant echelon cracks. *Geol. Soc. Am. Bull.* **93**, 1291–1303. (doi:10.1130/0016-7606(1982)93<1291: FAIODE>2.0.CO;2)
- 54. Ben-Zion Y, Sammis CG. 2013 Shear heating during distributed fracturing and pulverization of rocks. *Geology* **41**, 139–142. (doi:10.1130/G33665.1)
- 55. Rice JR. 2006 Heating and weakening of faults during earthquake slip. *J. Geophys. Res. Solid Earth* **111**, B05311. (doi:10.1029/2005]D005939)
- 56. Rice JR, Sammis CG, Parsons R. 2005 Off-fault secondary failure induced by a dynamic slip pulse. *Bull. Seismol. Soc. Am.* **95**, 109–134. (doi:10.1785/0120030166)